

Adaptive Sampling of 3D Spatial Correlations for Focus+Context Visualization

Christoph Neuhauser, Josef Stumpfegger, and Rüdiger Westermann



Abstract—Visualizing spatial structures in 3D ensembles is challenging due to the vast amounts of information that need to be conveyed. Memory and time constraints make it unfeasible to pre-compute and store the correlations between all pairs of domain points. We propose the embedding of adaptive correlation sampling into chord diagrams with hierarchical edge bundling to alleviate these constraints. Entities representing spatial regions are arranged along the circular chord layout via a space-filling curve, and Bayesian optimal sampling is used to efficiently estimate the maximum occurring correlation between any two points from different regions. Hierarchical edge bundling reduces visual clutter and emphasizes the major correlation structures. By selecting an edge, the user triggers a focus diagram in which only the two regions connected via this edge are refined and arranged in a specific way in a second chord layout. For visualizing correlations between two different variables, which are not symmetric anymore, we switch to showing a full correlation matrix. This avoids drawing the same edges twice with different correlation values. We introduce GPU implementations of both linear and non-linear correlation measures to further reduce the time that is required to generate the context and focus views, and to even enable the analysis of correlations in a 1000-member ensemble.

Index Terms—Correlation, chord diagrams, focus+context, ensembles, multivariate data.

1 INTRODUCTION

IN this work, we use chord diagrams with hierarchical edge bundling [2] for correlation visualization in 3D ensemble fields. By correlation we mean any statistical dependence measure between the values of one or two physical variables at selected locations in 3D space. However, since the space along the circular layout is limited, large numbers of entities cannot be well represented. While a chord diagram can at most show few hundreds of entities and their relationships, considerably more need to be shown to convey all point-to-point correlations in a 3D field.

To address this limitation, we propose using two chord diagrams which are shown side by side. The context view (see left of Fig. 1) uses a chord diagram that shows the correlations between all regions in the domain that emerge by partitioning space into disjoint sub-domains. The focus view (see middle and right of Fig. 1) shows refined correlations between exactly two selected regions. The user controls the refinement by selecting edges in the chord diagrams and can refine down to the level where point-to-point correlations are shown.

The correlation between two regions is indicated by the maximum of all point-to-point correlations between pairs of grid points in either region. In general, however, computing all point-to-point correlations between a pair of regions—and for all pairs shown in the context view—is unfeasible due to excessive computing times. I.e., for the ensembles we consider in this work, the computation of all point-to-point correlations using the Pearson Product-Moment Correlation Coefficient (PPMCC) as a linear dependence measure takes more than two days on a recent GPU, and the computation of more complex measures like the non-linear Mutual Information (MI) takes considerably longer. Storing all point-to-point correlations, on the other hand, requires more than 2.8 TiB of memory (assuming two bytes per correlation value) for a single variable and, thus, is unfeasible too.

Our strategy to reduce the time for generating the context and focus diagrams is twofold. Firstly, we provide efficient GPU implementations—especially for computing MI—to speed up the computation of single correlation samples. Secondly, and inspired by the approach of Chen et al. [3], we employ importance-based correlation sampling to significantly reduce the number of point-to-point correlations that need to be computed. However, we use Bayesian Optimal Sampling (BOS) to automatically select the set of point-to-point correlations that provide a good estimate of the maximum correlation between any two points from different regions. Especially the time required for generating the context view, where correlations between many pairs of large regions need to be estimated, can be reduced significantly via BOS. If the data does not fit into GPU memory, the system switches to an aggregate data representation using statistical means, at a resolution level that can be stored on the GPU. BOS is then performed on this level to avoid performance losses, at the expense of higher uncertainty in the maximum correlation estimates. Our main contributions are:

- Locally adaptive BOS is used to compute the maximum point-to-point correlation between two regions from only few correlation samples.
- A novel GPU implementation of point-to-point MI computations exploiting parallel search and sorting operations.
- Entities, i.e., domain regions or points, are arranged along the circular chord layout using a space-filling curve.

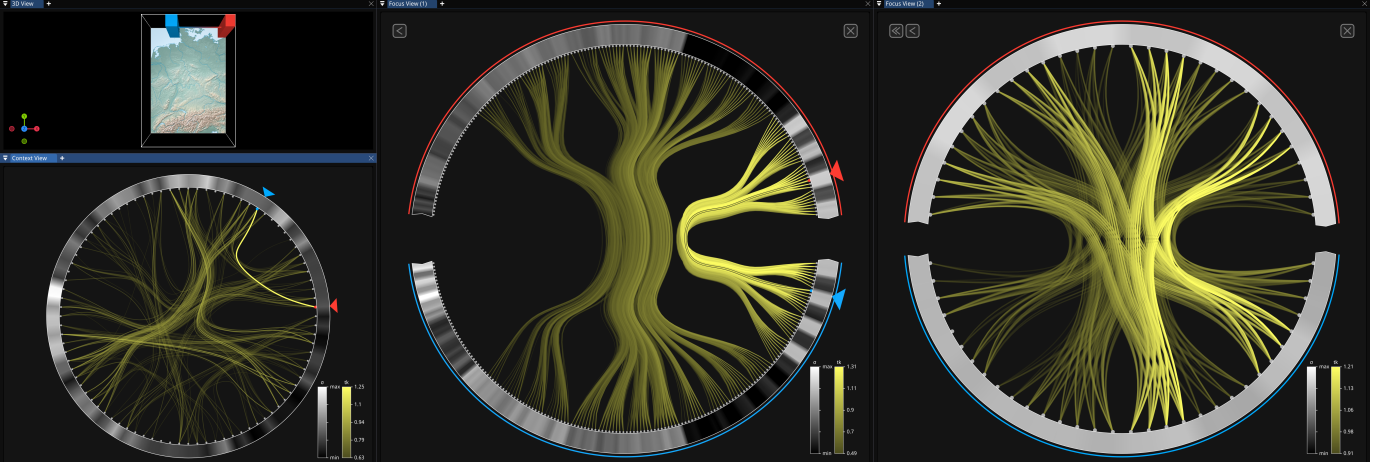


Fig. 1. Bottom left: Context view of a large weather forecast ensemble [1] shows mutual information (MI) maxima between regions in a 3D space partition, laid out on a chord along a space filling curve and visualized via edge bundling. The ensemble spread is encoded in the outer shell. Maxima are estimated via Bayesian optimal sampling (BOS) for all 3828 pairs of regions, each comprising $32 \times 32 \times 20$ grid points, in less than 16 seconds. Selected regions (red and blue triangle) are shown in a 3D view (top left). Middle: Focus diagram shows refined MI estimates - computed on the fly using our GPU implementation in less than 4 seconds - between selected regions. Right: Focus view on regions selected in the first focus diagram.

- A focus diagram shows a selected pair of regions opposite to each other on the circular layout.

Chord diagrams with hierarchical edge bundling have been selected for correlation visualization because they can effectively reduce the amount of displayed edges, and correlations below a user-selected threshold can simply be omitted. In correlation matrices, as an alternative, entries corresponding to low values can be left blank, but they are shown nevertheless and take up space. Thus, chord diagrams can more effectively reduce visual clutter. Furthermore, to be able to efficiently determine all major correlations for a selected entity, i.e., by following the corresponding row or column, the full correlation matrix needs to be shown. This requires showing redundant information for the symmetric correlation measures used in this work and is avoided when using a chord diagram. However, when correlations between two points and different variables are analyzed, it matters at which point which variable is considered. The same edge then needs to be drawn twice with different correlation strength in a chord diagram, leading to visual clutter. To avoid this, we show these correlations in a correlation matrix, which is then completely filled. Adaptive refinement is supported as described, by selecting matrix elements and showing the refined regions in a focus diagram using again a correlation matrix.

The remainder of this paper is structured as follows. After reviewing previous work, we describe and evaluate BOS for estimating the maximum correlation between two regions using a reduced set of correlation samples, and we introduce a novel GPU method for computing the MI between many pairs of random variables in parallel. Next, we introduce focus+context chord diagrams for correlation analysis in 3D ensemble fields. We then perform a quality and performance evaluation of the proposed approach, and demonstrate the use of the proposed approach with a synthetic and two large 3D weather forecast ensembles. The paper is concluded with ideas for future work.

2 RELATED WORK

In this work, we address the problem of how to efficiently visualize spatial correlations in large 3D ensembles of scalar fields. This is in contrast to many previous approaches for ensemble visualization, which have often been devoted to the visual analysis of the ensemble spread, using feature- and location-based approaches [4]–[6]. This includes approaches that provide visual abstractions of the major trends in ensembles of line or surface features [7]–[11], as well as location-based approaches that visualize local statistical data summaries [7]–[9] or find compact representations of ensemble data [12].

2.1 Ensemble Correlation Analysis

The analysis of spatial (auto)correlations, concerned with both time-varying and ensemble data, is an important task in meteorology and climatology. Nocke et al. [13] introduce concepts from visual network analytics to analyze climate networks. In particular, they use edge bundling in geo-referenced networks to indicate spatial correlations in 3D climate data. Wilks [14] discuss the effect of spatial correlations among the grid points on statistical significance tests in atmospheric sciences. They focus on the analysis of spatial correlations of linear trends in annual precipitation, and plot the correlations of pairs of cells with a certain maximum distance threshold as a scatter plot and fit a decay function to show the decrease of the correlation by the cell distance. For iso-contours in scalar ensemble fields, Ferstl et al. [15] assess the spatial correlation of their occurrence at different locations in the domain. Global teleconnections are visualized by Delalene et al. [16] to analyze in interannual to decadal climate variability. They use dependence measures to infer spatial functional networks between clustered sub-domains, in combination with correlation matrices to visualize such dependencies. Kumpf et al. [17] use correlation clustering to assess the sensitivity of numerical weather forecast quantities to changes in model variables. Their

approach aims to reveal the confidence in the sensitivities obtained via ensemble sensitivity analysis [18], [19], which is used in meteorology to determine the origin of forecast errors and improve placing of targeted observations. Evers et al. [20] introduce the use of multi-dimensional embeddings for determining clusters in time series correlation in 2D multi-field climate ensembles.

Besides linear correlation measures such as the Pearson correlation coefficient, non-linear measures like MI have been considered in atmospheric and climate sciences. Laarne et al. [21] use MI for exploring non-linear dependencies in atmospheric data. They use it both for analyzing temporal autocorrelations of a single field using line plots and correlations between multiple fields using static correlation matrices. Babel et al. [22] use MI for selecting the most suitable explanatory variables that are fed to a neural network for rainfall forecasting. Ning et al. [23] use MI for uncertainty assessment in precipitation forecasts.

2.2 Correlation Visualization

In particular for the analysis of multivariate data, where multiple variables are given at each data point, a number of approaches for correlation visualization have been proposed. The survey by He et al. [24] gives an overview of the different research areas in the field of multivariate spatial data analysis. One line of research is dedicated to the finding of appropriate similarity measures to support multivariate correlation analysis, such as gradient-based measures as introduced by Sauber et al. [25], Gosink et al. [26] and Nagaraj et al. [27]. Zhang et al. [28] introduce correlation maps, which show pairwise correlation between variables in a graph, and combine them with a parallel coordinate view indicating the main correlation structures on the data level. Liu and Shen [29] introduce probabilistic association graphs for the analysis of informativeness and uniqueness of multivariate data. Like in our work, their visual workflow provides a circular chord diagram for visualizing the relationships between pairs of entities. In some previous works [30]–[32], MI has been considered as a measure of statistical dependence between different variables.

Another popular approach for correlation analysis is correlation clustering. Pfaffelmoser and Westermann [33] cluster regions of 2D scalar fields based on a measure of the correlation of a random variable to its surrounding, called the correlation neighborhood. Liebmann et al. [34] use hierarchical correlation clustering in combination with a dendrogram visualization. Berenjkoub et al. [32] combine the segmentation of the spatial domain based on correlation strength with according coloring of pathlines, yet they restrict to correlations among pairs of attributes at narrow spatial regions and fixed locations over time or along pathlines. Evers et al. [35] combines a hierarchical correlation segmentation algorithm with correlation heat maps. Biswas et al. [30] cluster variables with similar distributions into groups and select a representative of each cluster. Variables are displayed in a diagram using a force-directed graph layout, where MI between two variables is used for computing the attractive force between two nodes. This graph view is linked with parallel coordinate plots and an isosurface view for further exploration. Due to its computational complexity, correlation clustering has been restricted to 2D fields so far.

To address the computational complexity of computing correlations, i.e., quadratic complexity in the number of entities to put into relation to each other, Su et al. [36] describe a system for parallel and distributed correlation analysis. The method generates a joint bin representation as a data aggregate on which measures like the MI can then be estimated efficiently. Chen et al. [3] propose using domain knowledge to first draw a set of samples from a simulation grid and compute the correlation volumes for each of these samples. A correlation volume stores the correlations from all points in the grid to a reference point. A matrix containing the distances of each pair of correlation volumes is then calculated and used to decide where more samples need to be computed.

2.3 Linearization of Spatial Data

Diagram techniques provide effective encodings of information in the form of schematic representations. When encoding the elements of a spatial domain like a grid in a diagram, the elements often need to be linearized to lay them out along curves or surfaces. When working with 2D or 3D spatial data, space-filling curves are often used to generate such a layout, i.e., a mapping of multi-dimensional positions to a one-dimensional index, under the objective that spatial proximity is preserved. Popular choices are Z-order curves or Peano-Hilbert curves [37]. Zhou et al. [38] introduce data-driven space-filling curves, which take into account the underlying data to increase the spatial proximity of elements with similar values. After linearization of the spatial elements, relationships between elements can be represented by connecting the linearized elements with lines. When displaying a lot of lines at once, the visualization can become cluttered due to many crossing lines and structures in the data become hard to perceive. Hierarchical edge bundling [2] partly alleviates this limitation by visually bundling lines based on a hierarchical structuring of the elements. In our work, we use a Z-order curve for linearizing the vertices of a 3D simulation grid. The advantage of Z-order curves over the data-driven curves by Zhou et al. [38] is that one can create an octree hierarchy over the elements, which can then be used for hierarchical edge bundling and on-demand subdivision of the displayed data level. A popular example demonstrating the use of diagram techniques with linearization of spatial elements is the work by Demir et al. [39]. After linearization, they use a histogram-based diagram view combining line and bar charts. Wang et al. [40] introduce a circular graph that can show the information transfer between pairs of variables. Recently, Weissenbock et al. [41] extend on the work by Demir et al. and propose to adaptively scale the mapping that is obtained via a space-filling curve, to enable focusing on important spatial regions.

Chord diagrams have been used in a number of previous works for the analysis of hierarchical data coupled with focus+context-like approaches. Rees et al. [42] propose a technique for the interaction with large chord diagrams, proposing brushing and deformed chord diagrams acting as focus views. Bae and Lee [43] combine chord diagrams with magnifying lens-like focus views for the analysis of the relation of tags. Gou and Zhang [44] describe a technique

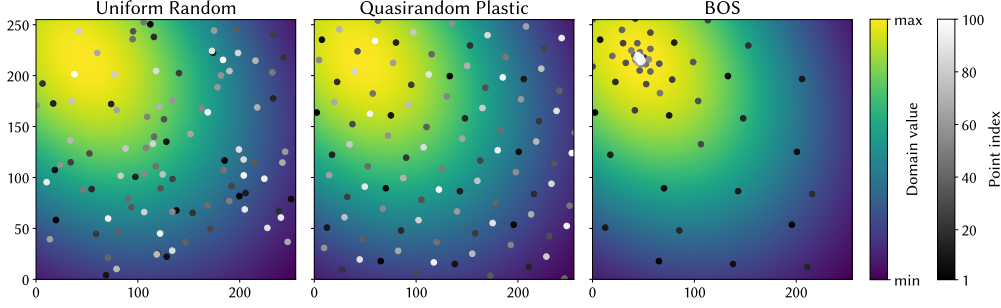


Fig. 2. Locations of the first 100 samples picked by different sampling schemes for finding the maximum in a 2D field, here the probability density function of a 2D multivariate normal distribution.

for the multiscale exploration of network data organized in a tree, where aggregate elements can successively be refined in the same diagram view.

3 CORRELATION SAMPLING

We assume that a simulation ensemble with E members is given on a 3D regular grid of size $X \times Y \times Z$. At every grid point, one or more variables are given per ensemble member. We further assume that M different entities can be encoded along the circular layout of a chord diagram, where M needs to be selected depending on the resolution of the diagram. Then, the Cartesian grid is partitioned into M sub-grids of size $C = X_d \times Y_d \times Z_d$. These sub-grids are subsequently called bricks. Partitions are built so that the maximum difference between any pair of elements from $\{X_d, Y_d, Z_d\}$ is minimized, i.e., bricks are mostly isotropic in the three dimensions. In the same way, each brick is recursively refined into $M/2$ bricks of ever smaller size, so that all siblings of exactly two bricks, i.e., the pair for which correlations are visualized, can be arranged along the circular chord layout. The refinement process is recursively repeated until bricks are comprised of one single data value.

To determine an indicator of the correlation between two bricks, point-to-point correlations between pairs of grid points in either brick are computed, and the maximum of these correlations is used. In the following, we describe the importance-based sampling strategy we employ to obtain a good estimator of these maxima from only a low number of effectively computed point-to-point correlations.

3.1 Bayesian Optimal Sampling

One approach for finding the maximum correlation between a pair of bricks is random sampling of correlations at grid points in each pair of bricks. One sample position corresponds to a position in a 6 dimensional space, where 3 dimensions represent the position in one brick, and the remaining 3 dimensions represent the position in the respective other brick. We have experimented with uniform random sampling and quasi-random low-discrepancy sequences, like Halton [45] and plastic [46] sequences. Previous works on the use of low-discrepancy sampling in quasi-Monte Carlo numerical integration [47] have shown superior convergence properties of quasi-random low-discrepancy sequences over random sampling. Unlike the case of Monte Carlo integration, we were not able to

perceive any significant differences in the convergence properties of uniform pseudo-random and quasi-random low-discrepancy sampling strategies for stochastic optimization. We have summarized our experiments in Section 5.3. However, a disadvantage of both random and quasi-random maximum sampling is that local or global maxima can be missed. This raises the question whether available samples can be used to infer in which regions new samples would be most likely to result in improved maxima.

Bayesian optimization [48], [49] aims to solve the optimization problem $\max_{\theta \in D} f(\theta)$ for a blackbox function f and domain D , which may be hard to compute. Underlying the optimization is the concept to minimize the number of function evaluations, i.e., the number of correlation samples that need to be computed in our scenario. The basic ingredients of the optimization are the probabilistic surrogate model and the acquisition function. While the former is used to express Bayesian belief about the outcome of the objective function that is derived from known evaluations, the acquisition function chooses the next sample to evaluate. Fig. 2 compares the specific sampling patterns used by (quasi-)random sampling and BOS for finding the maximum value in a 2D domain.

Specifically, Gaussian process surrogate models can be used to model a distribution of the function values for each location in the parameter space. To restrict the distribution of available functions to those that agree with the available correlation samples, the model is conditioned on the new sample and the given set of samples. We randomly sample an initial set of correlations and update the model accordingly. The acquisition function is then maximized with respect to the selected model, to predict the locations of the next correlation samples. For the acquisition function, we use the Upper Confidence Bound (UCB) [50], and for optimizing it, a randomized version of DIRECT-L [51] is used, which is provided via a binding to the NLOpt library [52]. We have evaluated all gradient-free optimization algorithms provided by NLOpt and found this optimizer to give the best error metric results in our concrete settings, see Section 5.3. The Matern kernel [53] is used for the covariance function of the underlying Gaussian processes.

Most Bayesian optimization algorithms operate on continuous search spaces. Daulton et al. [54] describe how to use probabilistic reparameterization, where the discrete search space of voxel center pairs is considered. As proposed by Daulton et al., we map continuous search space

parameters $\theta \in [0, X_d - 1] \times \dots \times [0, Z_d - 1]$ to discrete 6D grid positions $P_i = \lfloor \theta_i \rfloor + B_i$, $B_i \sim \text{Ber}(\theta_i - \lfloor \theta_i \rfloor)$. $\text{Ber}(p)$ is the Bernoulli distribution, which has an outcome of 1 with a probability of p and an outcome of 0 otherwise. Consequently, the continuous positions between voxel centers will be mapped to closer centers with higher probability. To obtain support for Gaussian processes and optimization, we integrate the library Limbo [55] into our application, and batch the acquisition of new correlation samples for multiple brick pairs using multiple CPU threads. This enables us to efficiently use GPU correlation computations in conjunction with Bayesian optimization on the CPU. Parallel executions on the GPU are exploited to compute correlations for multiple feature vectors simultaneously.

3.2 GPU-Accelerated Correlation Computation

Since the proposed workflow builds upon in-turn computations of large sets of point-to-point measures of statistical dependence, these computations need to be highly efficient to not hinder interactivity. In order to not restrict the workflow to computationally lightweight measures like PPMCC, a novel optimized GPU implementation for computing MI has been developed.

Cover and Thomas [56] define MI as the “relative entropy between the joint distribution and the product distribution” of two random variables, i.e.,

$$MI(X; Y) = H(X) - H(X|Y) = H(Y) - H(Y|X), \quad (1)$$

where X and Y are two random variables, and H is the entropy. Like PPMCC, also MI is symmetric in the two random variables, yet it is in the range $[0, \infty)$ and does not distinguish between negative and positive correlations.

While PPMCC requires merely to compute means and variances and can, thus, be realized efficiently on the GPU, MI requires to estimate the joint discrete probability density function from the joint histogram of the two variables in order to compute the conditional entropy. A popular approach for computing the joint histograms is via binning, i.e., the two continuous random variables are discretized and a joint and two marginalized histograms are computed for the discretized realizations. MI is then estimated from the discretized realizations. Binning has been both parallelized and ported to the GPU in previous works, e.g., for the purpose of correlation analysis [36] and medical image registration [57]–[60].

As has been demonstrated and analyzed by Kraskov et al. [61], however, binning introduces systematic errors and result in low fidelity estimators. To avoid this, they propose using entropy estimates that are derived from the Chebyshev distances between the k -th nearest neighbor in the joint distribution space. Given X and Y , the joint distribution $Z = (X, Y)$ is represented by joint 2D data samples $z_i = (x_i, y_i)$. For each joint sample z_i , its distance ϵ_i to the k -th nearest neighbor is calculated using the Chebyshev distance, i.e., for a k -th nearest neighbor z_j , $d(z_i, z_j) = \max\{|x_i - x_j|, |y_i - y_j|\}$. We choose $k = \lceil \frac{3n}{100} \rceil$ in accordance to the results by Kraskov et al. for correlated Gaussian distributions. Then, for a joint sample z_i the numbers $n_{x,i}$ and $n_{y,i}$ of joint samples fulfilling respectively $|x_i - x_j| < \epsilon_i$ and $|y_i - y_j| < \epsilon_i$ are computed, and the MI is estimated as

$\widetilde{MI}(X, Y) = \psi(n) + \psi(k) - \frac{1}{n} \sum_{i=1}^n \psi(n_{x,i}) + \psi(n_{y,i})$. Here, n is the number of realizations of the random variables, i.e., the ensemble member count E in our application, and the so-called digamma function $\psi(z)$ is the logarithmic derivative of the gamma function $\Gamma(z)$ [62], i.e.,

$$\psi(z) = \frac{d}{dz} \ln \Gamma(z) = \frac{\Gamma'(z)}{\Gamma(z)}. \quad (2)$$

Notably, due to the complexity of k -nearest neighbor search and frequent evaluations of the digamma function, only roughly 5000 point-to-point MI samples can be computed per second on the CPU for the largest of our data sets, compared to approximately 800000 per second using PPMCC (cf. Table 1). Since we are not aware of any GPU implementation of the Kraskov estimator (abbreviated as KMI in the following sections), we introduce such an implementation in the following. This implementation achieves a speed-up of a factor of 10, and thus gives the speed that is required for an interactive correlation analysis as intended by our approach.

At the core of an efficient computation of KMI is a data structure that allows to efficiently perform k -nearest neighbor queries for many joint samples in parallel on the GPU. Notably, the search data structure needs to be rebuilt for each pair of points for which MI is estimated, i.e., for each set of E joint data samples $z_i = (x_i, y_i)$, $i \in \{1, \dots, E\}$. Then, the data structure is used to determine the distance to the k -th nearest neighbor for every joint sample. In principle, k -d trees are well suited for this task, yet recursive tree traversal and heterogeneous code paths for different data samples in the tree construction and distance computation make an efficient GPU implementation challenging. Since the GPU is based on a single instruction, multiple threads (SIMT) model, where many threads are run in lockstep, it can only sequentially evaluate different code branches for a group of threads. Furthermore, to reduce latencies, as many memory access operations as possible should be moved outside of branches. Lastly, GPU shading languages usually do not support recursion, which is used in most available k -d tree implementations.

In a number of previous works, these restrictions have been addressed with specific adaptations of k -d tree construction and traversal on the GPU [63]. The use cases of these implementations, however, differ significantly from ours. While usually a single k -d tree representing an entire scene is built once and many queries are executed in parallel, in our scenario as many k -d trees as MI values need to be built, i.e., one k -d tree per pair of joint data samples. Then, each tree is used to accelerate the E k -th nearest neighbor searches for each joint sample z_i . Thus, in our implementation we assign the computation of one point-to-point MI value to one compute thread, so that a single thread computes its specific k -d tree and performs all k -th neighbor searches sequentially. As neighboring threads of a thread group will build and traverse k -d trees based on different data in lockstep, it is important to avoid divergence caused by the different data being processed per thread.

One of the most recent GPU-friendly k -d tree traversal algorithms by Wald [64] employs iterative stack-free tree traversal to avoid recursion and minimize diverging code

branches. Compared to a custom iterative k-d tree traversal using a manually managed stack as a replacement for recursion, the approach turned out to be about 15% faster for the large ensembles we consider in this work. However, when using the stack-free implementation we noticed that the fairly heterogeneous sets of data values assigned to the threads in one thread group can lead to significant execution divergence between neighboring threads during the sorting operation required for k-d tree construction. To reduce this effect, we have incorporated the GPU heap-sort implementation by Kern et al. [65]. Instead of using variable loop bounds and branching to avoid unnecessary element swap operations like sorting algorithms tailored to CPUs like quicksort [66], the proposed heap sort implementation accepts potentially unnecessary element swaps in favor of avoiding branching. By this, the computation of the MI is further accelerated by about 10% to 20% (depending on the ensemble size) compared to using an adapted, iterative version of introsort [67]. Introsort is a hybrid sorting algorithm switching from quicksort to another sorting algorithm when the data recursively sorted becomes too small for quicksort to work efficiently. Introsort is used, for example, by the GNU standard C++ library [68].

Finally, we use the Lanczos approximation [69], [70] in our implementation to efficiently evaluate the digamma function on the GPU in constant time. The Lanczos approximation is a method for the numeric approximation of the gamma function and can also be extended to the digamma function using the relationship between the two functions in Eq. (2). In Section 5.2, we compare the performance of our GPU implementation of KMI to an optimized implementation on the CPU, and observe speed-ups of approximately one order of magnitude.

3.3 Sampling from Spatial Aggregates

If the ensemble cannot be stored in GPU memory, sampling point-to-point correlations in the initial data becomes far more time consuming, since it requires streaming the entire ensemble when new samples are needed. Notably, however, for realistically sized data sets this affects only the generation of the context view, where many point-to-point correlations need to be computed for each pair of initial bricks. Once the user has selected a brick pair for analysis in the focus view, the initial data values of both bricks are quickly streamed to the GPU and BOS is performed as described.

To avoid the aforementioned restriction, a hierarchical ensemble representation using the same partitioning strategy as for brick refinement is computed first. We have evaluated both a mean-tree and a max-tree as alternatives. The mean/max-tree stores for each brick and each ensemble member—starting at the first refinement level—the means/maxima of all variables at the grid points represented by this brick. For the largest ensemble we consider in this work, this process takes about 12 seconds on our target architecture per variable. For computing the correlation with respect to a selected variable between a pair of bricks, BOS is then performed using the mean/maximum values at the highest resolution tree-level that just fits into GPU memory.

It is clear that using aggregate values for correlation estimation introduces errors in the estimated correlation

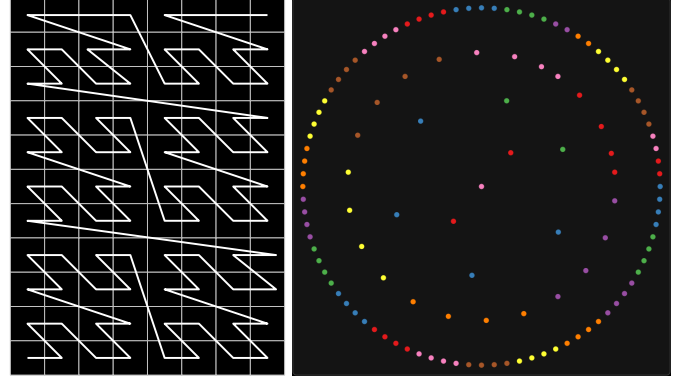


Fig. 3. Left: Subdivision of a $250 \times 352 \times 20$ simulation grid into $8 \times 11 \times 1$ bricks of size $32 \times 32 \times 20$. The bricks are traversed using a Z-order curve. Right: Nodes in the chord diagram. The leaves ordered by the Z-order curve are linearized in the outermost circle. Inner octree nodes used for hierarchical edge bundling (they are hidden during rendering). Nodes with the same parent are assigned the same color.

maxima, because significant and in particular isolated high correlations can be overlooked. On the other hand, our experiments show that performing maximum correlation estimation on pre-computed means gives results that are close to those obtained via BOS and sampling point-to-point correlations from the initial data. Furthermore, when showing the ensemble spread in the chord diagrams as described below, this information indicates those bricks where the estimation is uncertain and further refinements should be performed. As our experiments have indicated that both the mean- and max-tree give more or less equal accuracy, we have decided to support the mean-tree in our implementation.

4 CHORD DIAGRAMS FOR 3D FIELDS

As discussed above, the ensemble domain is partitioned into M regions, and each region is again partitioned into $M/2$ sub-regions. M is the number of entities that can be encoded along the circular layout of a chord diagram, and it needs to be selected depending on the resolution of the diagram. For instance, when plotting a chord diagram on a 512×512 viewport, we typically choose $M = 128$ to approximately have 4-7 pixels between each entity on the circle so that edges between entities can be well distinguished.

Bricks are laid out along the circle through a Z-order curve (see Fig. 3 left), so that the spatial proximity of bricks is preserved as good as possible in the circular layout. Unlike other space-filling curves, like the data-driven approach by Zhou et al. [38], Z-order curves have the property that when the data is hierarchically partitioned using an octree structure, all siblings of a node are visited by the space-filling curve before proceeding to the next parent node. Since we use such an octree layout for brick refinement, and also build an octree-based partition above the initial M bricks in turn, we can effectively make use of hierarchical edge bundling [2], i.e., bundling lines based on a hierarchical structuring of the entities on the circular layout. By using a linearization of bricks along a Z-order curve, we directly obtain a hierarchy for the bricks that are visualized in the chord diagram. The root node of the

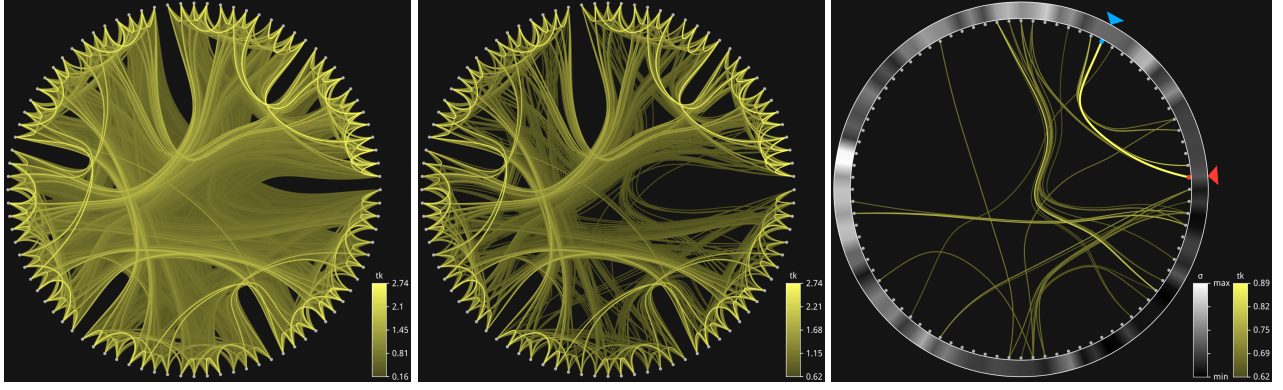


Fig. 4. Context chord diagram using MI as dependence measure for a large simulation ensemble [1]. Left: Spatial correlations in the temperature field t_k . Middle: Sub-selection of correlations with $MI \geq 0.62$. Right: Sub-selection of correlations with brick distance $\geq 570\text{km}$ (measured from the brick centers) and $MI \geq 0.62$. Ensemble spread σ of t_k is shown on the outer ring.

octree is placed in the center of the chord diagram and the inner nodes are positioned from the center to the outer perimeter of the diagram. The angle of an inner node is the average of the angles of their child nodes. This hierarchical arrangement is demonstrated in Fig. 3 right. Finally, as proposed by Holten [2], when connecting two entities (i.e., leaf nodes of the octree) the inner nodes along the shortest path between the two leaves are used as control points for constructing a smooth B-spline curve, i.e., an edge. B-splines are discretized using the de Boor algorithm [71] and rendered using the vector graphics library NanoVG [72].

4.1 Context Chord Diagram

In the context diagram, the M bricks, each representing a sub-grid of size $X_d \times Y_d \times Z_d$, are aligned along the circular chord layout. They are visualized via small circles and connected by edges indicating their pair-wise correlations. Each edge represents the maximum correlation between any of the grid points in two connected bricks (see Fig. 4). The user can select showing correlations in a selected range, to emphasize important relationships. Furthermore, only correlations between bricks in a certain distance range can be shown, which enables to switch between long-, mid- and short-range correlations. Edges are ordered with respect to increasing correlation magnitude, to also emphasize strong negative correlations, and rendered in this order on top of each other. Correlation strength is mapped to color, starting at the background color (low strength) and fading towards a selected key color (high strength). The user can specify a range of correlation values to use for filtering the displayed edges. By default, the selected range is also used as the range for color mapping.

As shown in Fig. 4 right, the outer ring around the circular layout is used to display additional ensemble information via a greyscale colormap, i.e., the per brick ensemble spread (average of the standard deviation σ). Since high ensemble spread indicates a high uncertainty in the ensemble simulation, the spread hints at interesting regions for further analysis and, in particular, indicates the uncertainty when estimating brick-to-brick correlations using mean values over successively refined sub-regions.

4.2 Focus Chord Diagram

When selecting an edge in the context chord, the correlations between the entities in the two bricks connected by this edge (called bricks A and B in the following) are displayed in finer detail in a new chord diagram—the focus chord diagram. While the context diagram displays the correlations between all $M(M-1)/2$ pairs of M initial bricks, the focus diagram displays the $M/2$ refined bricks of A on the bottom semicircle and the $M/2$ refined bricks of B on the top semicircle of the circular chord layout. Self-correlations within A and B are not considered, as selecting an edge indicates a user’s interest in a finer representation of the correlations between the two connected regions, but not necessarily the self-correlation within these regions. The selection triggers the refinement of A and B into M smaller bricks and $M/2 \times M/2$ pairs for which correlations are computed and edges are drawn. For computing the correlations, correlation sampling is used as described in Section 5.4. The ring is again colored via the ensemble spread in each of the smaller bricks.

As shown in Fig. 5 right, by first selecting an edge in the context view and then subsequently selecting edges in the focus view, the user can adaptively navigate down to the finest resolution level. The focus chords, however, are not shown side by side, but each newly refined chord replaces the currently seen one. To show the refinement level, as many navigation buttons (visualized via arrow symbols) are shown as the number of times the user has selected a refinement. By clicking a buttons, the user can jump back in the hierarchy by the number of levels that is encoded into the arrow symbols.

Each selected brick is laid out along one semicircle using a local Z-curve, as shown in Fig. 5 (left). To indicate which bricks have been selected for refinement in the context view, two arrows in blue and red are used to mark these bricks. Accordingly, the top and bottom semicircle in the focus view are visualized using a blue or red outline (cf. Fig. 5 (right)). The spatial regions corresponding to the selected bricks are put into spatial context in a 3D view, by drawing them as opaque boxes with the size and at the locations of the selected bricks. The 3D view is updated whenever the user either selects an edge or hovers over an edge with the mouse cursor in the context or focus view.

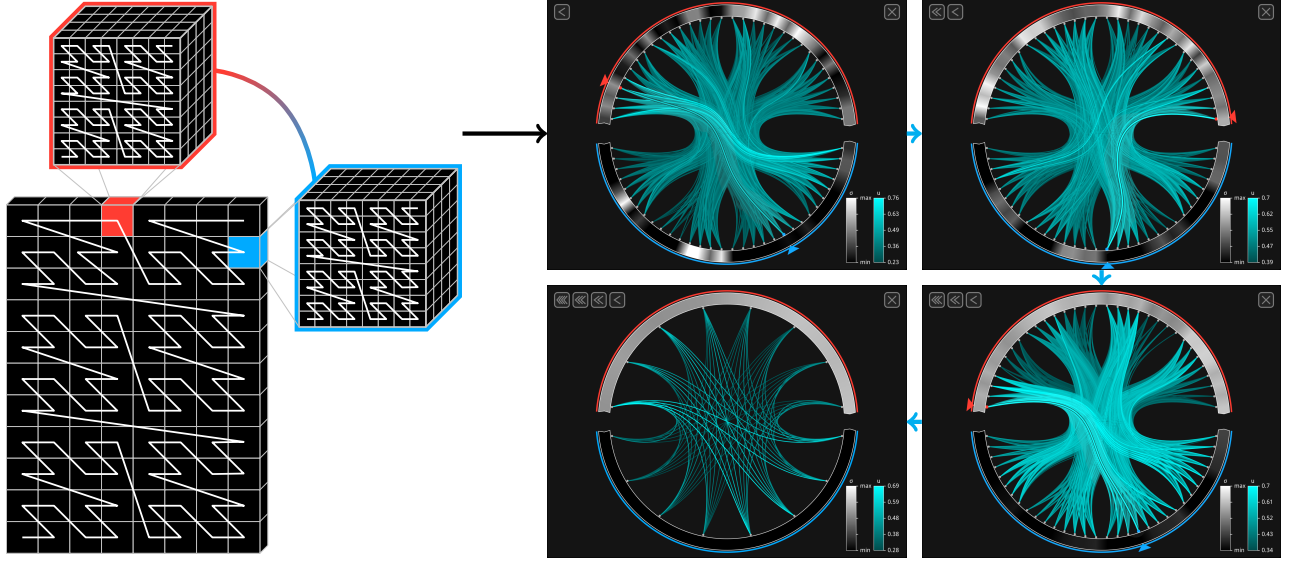


Fig. 5. Recursive linear layout of bricks along a z-curve. Two bricks are selected (red and blue), and laid out on the respective upper and lower half-circle in the top left focus view. Entities in each brick are linearized via a z-curve. In further refinements of the focus view (indicated by blue arrows), the picked regions are again laid out along z-curves.

In case the user is interested in refining only one single brick, i.e., to specifically look at self-correlations in this brick, the small circle representing the brick in the context or focus diagram can be clicked. In this case, the new focus diagram is generated as previously described, yet now the refined bricks of the selected one are shown along the top and bottom semicircle in the focus view.

4.3 Comparative Correlation Visualization

The proposed workflow for correlation sampling and visualization can be used directly to compare spatial correlations in two different fields, i.e., two different simulation variables. In this case, each brick is duplicated to also represent the second variable field, and the edges of the different variables are rendered into the same chord diagram with different colors.

Since edges showing different variables can occlude each other they are sorted with respect to (absolute) correlation strength and rendered in the order of increasing strength. Thus, edges indicating higher correlation are blended on top of curves with lower correlation. This is demonstrated in Fig. 6 left. Furthermore, a second ring is shown in the chord diagram to indicate the ensemble spread with respect to a second variable, enabling an effective comparison of the spatial distribution of the spread.

In addition to showing edges that indicate correlations in a single variable field, it is interesting to analyze the correlations between two different variables. BOS (or sampling on aggregates) is then performed as described, but point-to-point correlations are computed between pairs of points from either field. When a chord diagram is used to visualize these correlations, however, the same edge is displayed with different correlation strengths, i.e., to indicate the correlation between the first and the second variable at, respectively, the first and the second point, as well as the correlation between the first and the second variable at, respectively, the

second and the first point. To avoid this, we show variable-to-variable correlations in a correlation matrix instead of a chord diagram. This matrix, which we subsequently call inter-variable correlation matrix, is completely filled due to the mentioned anti-symmetry and does not show redundant information (see Fig. 6 right). Once the system switches from a chord diagram to an inter-variable correlation matrix, adaptive refinement is supported as described. By selecting a matrix element, the refined regions are shown in a focus diagram using again a correlation matrix.

5 ANALYSIS AND RESULTS

5.1 Data Sets

In the following, we analyse the proposed correlation visualization using three different data sets: “Synth” is a synthetic 3D ensemble comprising 1000 members at a grid resolution of $256 \times 256 \times 32$. It contains two correlation clusters in different domain regions. Each cluster itself is comprised of a larger and few smaller clusters (cf. Fig. 9 bottom). Within each cluster, the correlations are positive, decaying by their l_∞ -norm distance from the cluster center (i.e., $\max\{d_x, d_y, d_z\}$). There is also high mutual correlation between each pair of clusters. Between clusters there are regions with low correlations to any of the clusters. “Necker” [1] is a convective-scale 1000 ensemble member simulation forecast over central Europe, using a “full-physics non-hydrostatic regional model (SCALE-RM) with a horizontal grid spacing of 3 km”. The values are stored on a regular grid of size 250×352 with 20 vertical height levels that capture vertical variations. The ensemble comprises multiple physical variables, such as temperature, wind speed, hail and precipitation. “Matsunobu” [73] is a large ensemble that has been simulated using the ICON-D2 numerical weather prediction model. It stores 180 ensemble members at a grid of size 640×704 with 64 vertical height levels. While “Necker”—even when two variables

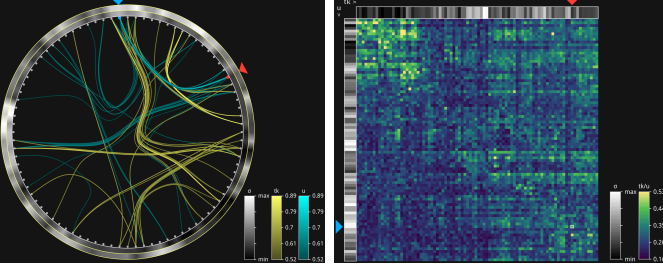


Fig. 6. Left: Comparative visualization of MI in temperature t_k and longitudinal wind component u of a weather forecast ensemble [1]. Right: Inter-variable correlation matrix showing correlations between t_k and u . Entries in the upper right triangular structure indicate correlations between t_k at first region (column) to u at second region (row), and between u at first region (row) to t_k at second region (column) for the lower left triangular structure.

are compared—fits entirely into the memory of our target GPU, this doesn’t hold for “Matsunobu”. Thus, the mean hierarchy described in Section 3.3 is used in this case to generate the context view.

5.2 Performance Evaluation

For PPMCC and KMI, Table 1 shows the performance that is achieved on the CPU and the GPU. All timings have been evaluated on a system running Ubuntu 20.04 with an AMD Ryzen 9 3900X 12-core (24-thread) CPU and an NVIDIA GeForce RTX 3090 GPU. The experiments have been performed with “Necker”, by selecting a grid point in the 3D domain and computing the correlations to all other grid points. This amounts to 1.76 million correlation computations, using 100 and 1000 members, respectively.

For computing KMI on the CPU, a parallelization is used that allocates dynamic heap memory outside of the parallelization loop. This avoids expensive system calls which affect the performance in every loop iteration. All CPU implementations utilize OpenMP for parallelization. The GPU implementation of KMI shows a considerable speedup of approximately $11\times$.

For the 1000 member ensemble, the throughput even for the computationally most expensive measure KMI is about 49000 samples per second. Notably, however, this throughput cannot be achieved with any of the tested sampling methods. The reason is that the one-to-many query is extremely cache-friendly and can effectively exploit SMT parallelism on the GPU. Furthermore, when used in combination with chord diagrams, computed correlations need to be downloaded to the CPU for generating the diagrams. In practice, a throughput between roughly 18000 samples per second is achieved for random sampling. BOS achieves a throughput of 11000 samples per second for BOS at 100 samples per brick pair and 8300 at 400 samples per brick pair. When using BOS, it is in particular the computational overhead that is introduced by the evaluation of a Gaussian process model that leads to the reduction, which scales non-linearly with the number of samples added to the model.

The situation is slightly different for the data set “Matsunobu”, which cannot be stored entirely in GPU memory. Thus, the system estimates correlations from the level where $2 \times 2 \times 2$ data values are represented by their means. Then,

TABLE 1
Performance comparison of CPU and GPU implementations of PPMCC and KMI. All correlations from a single reference point to all other 1,760,000 grid points in “Necker” are computed. n is the number of ensemble members.

	Measure	CPU (s)	GPU (s)	Speedup
$n = 100$	PPMCC	0.049	0.002	24.5x
	KMI	6.085	0.672	9.1x
$n = 1000$	PPMCC	2.1	0.21	10.0x
	KMI	412.2	35.9	11.5x

the entire data set fits into GPU memory and the context diagram can be computed in approximately 15 seconds.

5.3 Qualitative Evaluation

Firstly, we evaluate the sampling strategies introduced in Sec. 3 for computing representative correlation maxima between pairs of bricks. For comparing the quality of different sampling strategies, it is necessary to compute the ground truth beforehand, i.e., the minimum and maximum of all point-to-point correlations between any pair of grid points in two bricks. Then, the relative error of the sampled maxima can be computed as the fraction of the difference between the maximum and minimum. However, for bricks of size $32 \times 32 \times 20$, as, for instance, used to generate the context view of “Necker”, this already amounts to more than 400 million point-to-point correlations that need to be computed for a single pair of bricks. Since in the statistical evaluation we consider averages over many pairs of bricks, this is unfeasible due to time constraints. On the other hand, considerably smaller brick sizes, for which the ground truth can be computed in a reasonable amount of time, are no longer representative. Consequentially, for evaluation with a real data set as shown in Fig. 7 left and middle, we show the convergence rates with increasing number of samples and increasing time budget that are achieved with different sampling strategies. The ground truth to which the sampling schemes converge is not known. In these experiments, the Kraskov MI estimator is used with “Necker”.

As can be seen in Fig. 7 left, for an equal amount of samples, BOS comes significantly closer to the assumed maximum than all alternative sampling variants. The resulting curve is steeper and indicates faster convergence to the ground truth than those of the alternatives. To confirm that the lower number of samples required by BOS is not outweighed by higher computation times for each sample, Fig. 7 middle shows the estimate of the maximum for given time budgets. Notably, BOS achieves higher accuracy than all other variants in the same amount of time, despite the fact that BOS samples are considerably more expensive as shown in the performance analysis before.

To further assess the convergence properties of all sampling method, we have designed a synthetic data set so that for each pair of bricks the minimum and maximum can be computed analytically. In particular, we choose the probability density function of a 6-variate normal distribution for generating the data set. Both the minimum and maximum of this function can be computed in constant time. After discretization, the maximum is always located at one of the 2^6 voxels closest to the mean and the minimum is located in

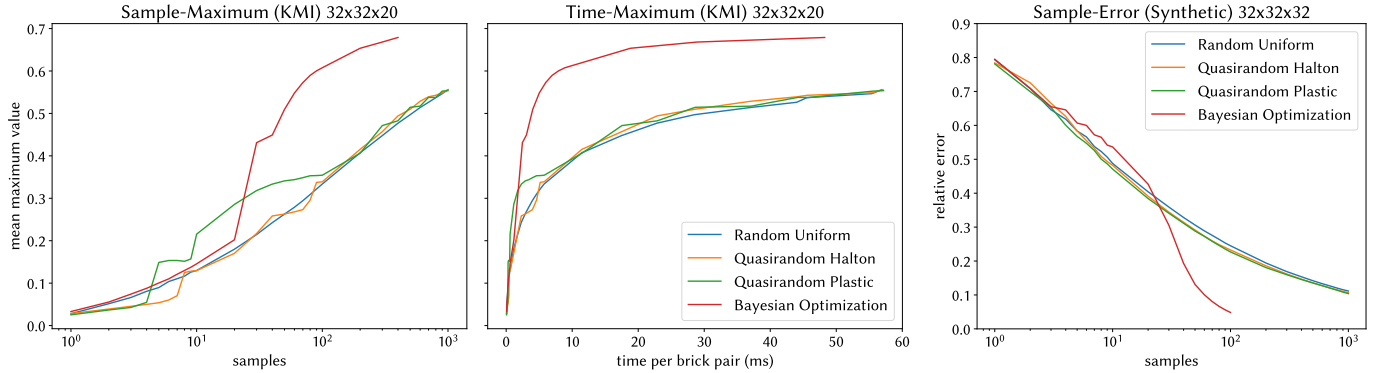


Fig. 7. Left and middle: Correlation sampling via BOS and random sampling variants. Mean sampled maximum for all brick pairs of $32 \times 32 \times 20$ voxels in “Necker”. Higher maximum is better. All observations are averaged over 10 runs. BOS achieves not only higher maxima for the same amount of samples, but also in a shorter amount of computation time. Right: Mean normalized error for 1000 randomly selected brick pairs of $32 \times 32 \times 32$ voxels for synthetically generated fields of multivariate Gaussians. Lower error is better. After an initial lead of random sampling, BOS for 100 samples is able to converge to an error of almost zero.

one of the corners of the 6-dimensional box-shaped domain. The mean is drawn using a uniform distribution from the interior of the box.

As shown in Fig. 7 right, BOS outperforms all other variants in convergence to the exact maxima. Here, the y-axis shows the mean relative error of the computed maxima. For each approximated maximum obtained via sampling, we compute the normalized relative distance on the scale from the exact minimum and maximum for the specific brick pair. A value close to 1 indicates that the sampling method is close to the minimum on average, and a value of 0 that it is close to the maximum. It can be seen that, on average, random sampling gives slightly better results than BOS for a low number of samples. BOS, on the other hand, shows the trade-off between exploration and exploitation. Exploration means searching in previously relatively unexplored areas with high uncertainty for possibly higher maxima. Exploitation means refining an already known good maximum to find a possibly higher value in its surroundings. For the synthetic data set, the acquisition function used by the Bayesian optimizer might prioritize exploration in the beginning. Since the data set is smooth and has a single local maximum, this only seems to pay off for a higher number of samples.

Furthermore, we evaluate the accuracy of correlation sampling when brick-to-brick correlations are computed via BOS on mean values instead of the initial data values. The maximum correlation between 1000 randomly sampled brick pairs of size $32 \times 32 \times 20$ in “Necker” is computed using BOS with 100 samples. BOS is performed on the initial data values, and on brick pairs of size $16 \times 16 \times 10$ and $8 \times 8 \times 5$ where respectively each entry contains the mean of $2 \times 2 \times 2$ and $4 \times 4 \times 4$ initial data values. All brick-to-brick correlations are computed 10 times and then averaged to reduce the effect of random initializations of BOS. The brick pairs are then sorted with respect to increasing maxima when computed on the initial data, and the maxima that have been computed on mean values are arranged accordingly. The results are shown in Fig. 8, demonstrating that even at a downsampling factor of four the maxima that are computed on the corresponding mean values are in good agreement with the maxima computed on the initial data.

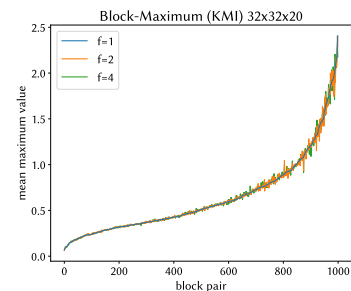


Fig. 8. Sampled correlation maxima in 1000 brick pairs from “Necker” (averaged over 10 runs) using the initial data ($f = 1$) and means of $2 \times 2 \times 2$ ($f = 2$) and $4 \times 4 \times 4$ ($f = 4$) data values in the temperature field τ_k . Brick pairs are sorted wrt increasing maxima in the initial data to reduce spikes. The average deviation for $f = 2$ and $f = 4$, respectively, is 1.6% and 1.7%.

At the same time, even at a downsampling factor of two the memory requirement is reduced by a factor of eight, so that “Matsunobu” can be stored entirely in GPU memory.

5.4 Sampling Strategy

Our tests confirm that even though BOS samples are more expensive than samples taken via random sampling, BOS requires so much less samples that overall the same quality is achieved in less time. However, when repeating the experiments with ever smaller bricks, the performance gains of BOS become less and less significant. In particular, while a noticeable advantage of BOS can still be perceived at a brick size of $16 \times 16 \times 16$, beyond that the random sampling approaches become more efficient at equal quality. This is because the data values in smaller bricks tend to have lower variation, in general, and the overall number of required samples becomes so low that the computational overhead of BOS cannot be amortized.

According to this observation, we pursue the following strategy. BOS is used to estimate the correlation maxima between the many pairs of large bricks at the context level. For instance, at the context level of “Necker” there are 8×11 bricks of size $32 \times 32 \times 20$, so that $88 \times 87 / 2$ brick-to-brick correlation maxima need to be estimated. With BOS using 100 samples per brick pair and KMI as correlation measure,

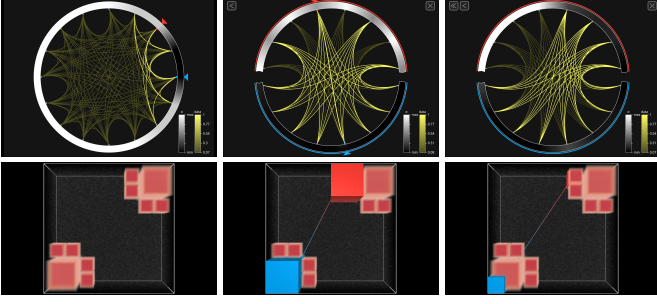


Fig. 9. Correlation analysis in “Synth” using the PPMCC. Left: Context view (top) shows sparse brick-to-brick correlations. 3D spatial view (bottom) confirms sparsity via volume rendering of the per-point correlation maxima. Red and blue triangles indicate bricks selected for refinement. Middle: Selected bricks are shown via red and blue cubes in the spatial view (bottom). Bricks contain different amounts of points with high and low correlations, resulting in different sparsity patterns in the focus view (top). Right: Second refinement shows asymmetric pattern on top half-circle, which is due to level-wise layout of data points along the z-curve.

this requires roughly 16 seconds of pre-processing time. Notably, it would take about 365 days to compute the brick-to-brick maxima if all point-to-point correlations were to be considered. At focus levels, and at latest if the brick size goes below $16 \times 16 \times 16$, the system switches to random sampling down to the level where the computation of correlations between all point-to-point pairs is fast enough. Here we consider an update time of less than 5 seconds to be acceptable.

5.5 Correlation Analysis

5.5.1 “Synth”

In our first experiment, we demonstrate the use of chord diagrams with BOS for an interactive analysis of the PPMCCs in “Synth”. Since the correlations in “Synth” are known (see Fig. 9 bottom left), the experiment demonstrates the potential of our approach to reveal these structures and hint towards the most prominent spatial relationships. “Synth” has been partitioned initially into $4 \times 4 \times 1$ bricks which are laid out along the context chord (see Fig. 9 top left). Only few edges between a small subset of all bricks indicate high correlation, i.e., between those bricks that contain (parts of) a cluster. The user can interactively select edges to see where the bricks with low or high inter-brick correlation are located in the 3D domain. When selecting an edge in the context chord, the two bricks connected via this edge are shown in the spatial view and laid out along the half-circles of the first focus chord diagram. For the two selected bricks, the focus view shows asymmetry in the number of entities showing large correlations between the upper and the lower half-circle. This occurs because an edge has been selected in the context view that connects a region densely filled with a large cluster with a region containing two smaller clusters, i.e., correlations are between all sub-regions in the brick containing the large cluster and only a subset of sub-regions in the other brick. When going further down in the hierarchy by selecting an edge in the focus diagram, one again sees in the second focus diagram (Fig. 9 top right) that both selected bricks comprise different numbers of finer bricks with high correlations.

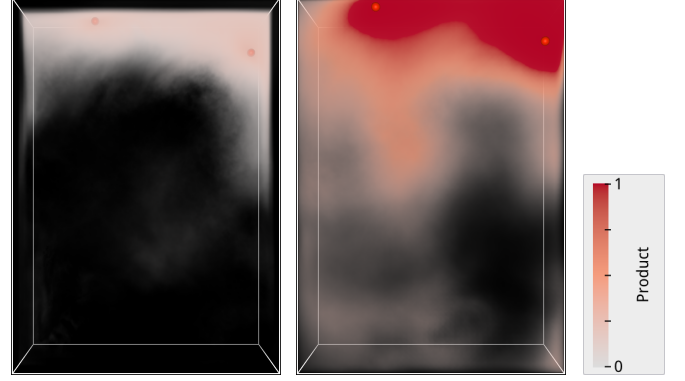


Fig. 10. Data set “Necker”: At each grid point the MI in temperature τ_k between this point and the two points marked by red dots are multiplied and volume rendered. The two points correspond to the locations of the selected bricks in the context view in Fig. 1. Left: MI in vertical layer 10. Right: MI in vertical layer 19.

Notably, in all situations BOS can correctly estimate the maximum PPMCC of 1 between all bricks containing parts of the clusters. Furthermore, it can be observed that the correlations are high where the ensemble spread is low, and vice versa. This is indicated by the spread shown around the circular layout, which is due to how the synthetic data set has been created. In regions outside of the red clusters in the 3D view, ensemble values are drawn from independent and identically distributed random variables, and values are more and more linearly distributed the closer they get to a cluster center.

5.5.2 “Necker”

In a second experiment, we analyse long-range MI structures in the temperature field τ_k of “Necker”. Therefore, we first suppress all correlations between bricks that are closer to each other than a selected distance threshold. A brick size of $32 \times 32 \times 20$ is used in the context view, so that all vertical levels are spanned by one brick. The focus view uses a brick size of $4 \times 4 \times 4$. This setting has been used to generate the visualizations in Fig. 1.

The context view reveals multiple regions which are connected by bundles of edges indicating high correlations. One bundle that stands out is seen on the top right of the diagram. A representative edge from this cluster has been selected (indicated by the red and blue triangles), and the corresponding bricks are shown in the 3D view and further subdivided in the focus view. The selected bricks lie over the Baltic and North Sea. As can be seen in the focus view, there are 32 entity pairs with notably high correlation. By hovering over the edge with the mouse, one can see that these entities correspond to the sub-regions in the topmost vertical levels. This confirms the observation by Necker and co-workers of low correlation between levels close to the ground and the tropopause, respectively. High correlations between spatially distant layers are not present.

When interactively hovering over the edge close to the selected one, it can be seen that τ_k has higher correlations in higher vertical layers. Furthermore, a cluster of high correlation—corresponding to the inspected bundle of edges in the context view—resides in the top right corner of the 3D field. These structures are confirmed in the volume

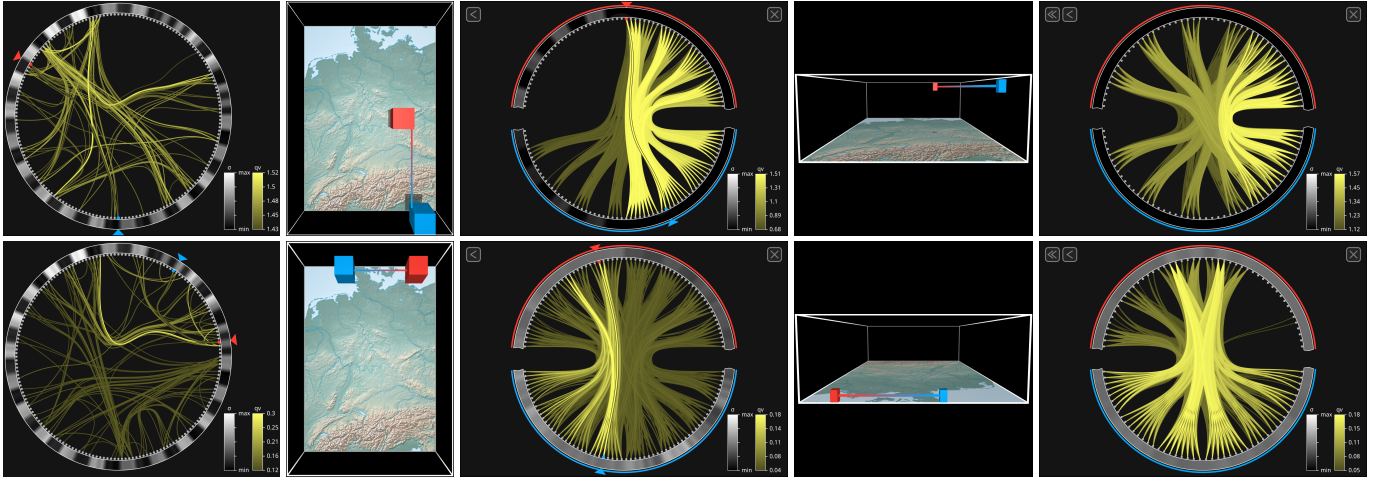


Fig. 11. Data set “Necker”: Visual analysis of MI in water vapor mixing ratio q_v . Top, left to right: Context view showing correlations between bricks with distance $\geq 288\text{km}$ and $MI \geq 1.43$, spatial view of selected brick pair, focus view of correlations between selected bricks, spatial view of refined bricks selected in focus view, focus view of correlations between selected refined bricks. Bottom, left to right: Same as top, but correlations with $MI \leq 0.3$ are shown.

renderings of 3D MI fields in Fig. 10, where MI values are computed separately between each grid point and two selected points. At each grid point, the two MI values have then been multiplied to indicate those regions where MI is high with respect to both selected points. As can be seen, higher correlations are revealed both in the most northern parts of the domain and in higher layers of the atmosphere. Overall, the proposed chord diagrams can effectively convey correlation structures over multiple scales in one single view. Notably, this could only be seen in correlation volumes by manual selection of many reference points.

In a second experiment, we analyze the spatial correlation structures in a different variable, the water vapor mixing ratio q_v (kg kg^{-1}), in Fig. 11. Most interestingly, when filtering for the highest correlations in Fig. 11 top, and in contrast to the findings regarding the temperature t_k , correlations between the North and Baltic Sea are mostly absent in the context view. As can be seen, e.g., from the picked pair of bricks in the context view, spatial correlations for q_v are higher over continental Europe. For the context view bricks spanning half of the height of the domain have been chosen. From the ensemble spread displayed in the outer ring it can be seen that the spread in lower levels is higher than in higher levels, conveyed through the striped pattern. We have selected two bricks for closer inspection over central Germany (red) and northern Italy (blue). The highest correlations in the focus view are all confined to the highest vertical layers, with some lower correlations also to medium layers above northern Italy. This becomes visible through hovering over the high-value edges running from bottom right to top right in the focus view. At these heights, q_v is highly correlated across large regions of continental Europe. When looking at a second focus view for a pair of selected sub-bricks (Fig. 11 top right), we see high symmetry of the correlation structure between the two regions.

In Fig. 11 bottom, we now filter for lower correlations ($MI \leq 0.3$) to also inspect lower correlations closer to the ground. In this case, the highest correlations are now again in the region over the North and Baltic Sea. For the

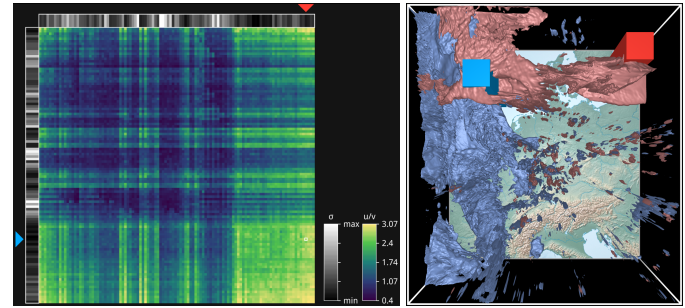


Fig. 12. Left: Inter-variable correlation matrix showing MI as dependence measure between the longitudinal and latitudinal wind components u and v in “Matsunobu”. Right: Spatial view with selected locations and isosurfaces for u (red) and v (blue) in a representative ensemble member.

bottom layers over the ocean, the correlation structures look significantly different than those over continental Europe. While they are significantly lower, the maximum is closer to the sea level. This can again be verified by hovering over high-value edges in the focus view. In the second focus view (Fig. 11 bottom right), two sub-bricks close to the ground have been selected. The blue sub-brick is closer to the coast than the red one. Here, we no longer have the perfect axis symmetry from the correlations of higher levels. A few of the sub-bricks in the red region are correlated to almost all of the sub-bricks in the blue region.

5.5.3 “Matsunobu”

In a third experiment, we first analyze the cross-correlations between the longitudinal u and latitudinal v wind components in “Matsunobu”. Fig. 12 left shows the corresponding inter-variable correlation matrix. An entry is marked with a red and blue arrow, and the selected bricks are shown in the spatial view in Fig. 12 right. The matrix view conveys a distinct cluster with high correlation values. Bricks in this cluster are mostly located in the western and northern parts of the simulation domain, which is seen in the spatial view when hovering over the matrix elements. Furthermore, iso-

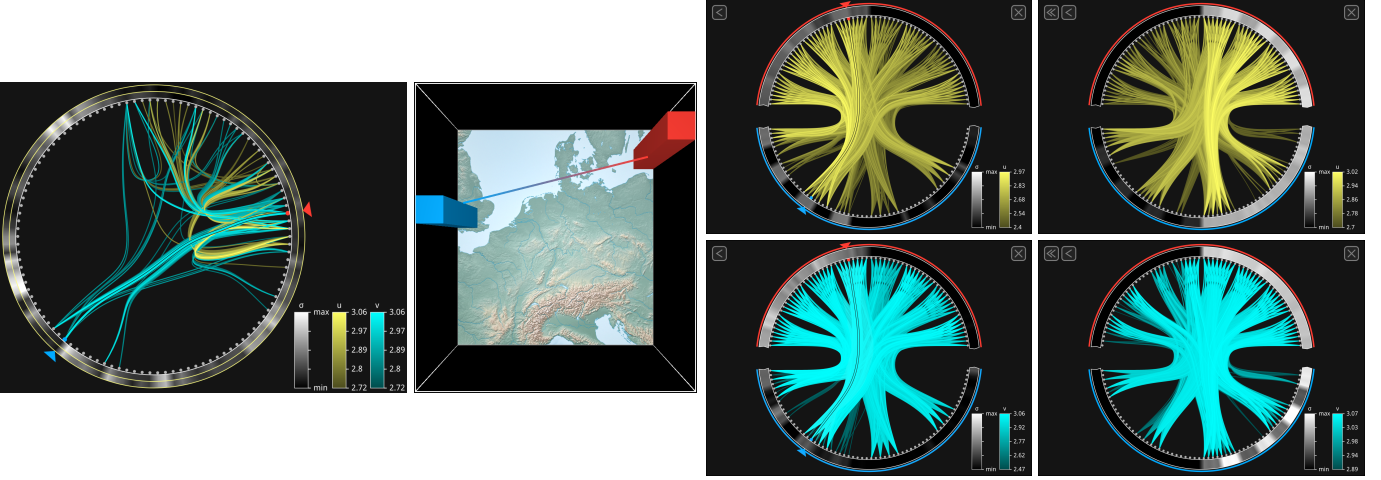


Fig. 13. Comparative chord visualization of MI in each of the variables u and v in “Matsunobu”. Left: Context diagram showing edges for brick distances $\geq 420\text{km}$. Middle: Spatial view of selected brick pair. Right: Focus diagrams for the first and second refinement levels.

surfaces in u (red surface) and v (blue surface) corresponding to high wind speed are rendered in the spatial view. They indicate a strong wind current in the northern and western parts. The standard deviations displayed next to the topmost matrix row and leftmost column show relatively low deviation between the individual ensemble members in the prominent cluster, hinting at high prediction accuracy. The high cross-correlations indicate that the individual ensemble members are strongly dependent. It is also conveyed that differences in the longitudinal and latitudinal wind components are considerably less correlated in the other regions over central Europe.

We then shed light on the correlation structures in u and v by means of a context chord diagram (see Fig. 13). Again, correlations are highest in the western and northern parts over Europe. In the context view, edges for both variables are rendered jointly, sorted from front to back by their corresponding correlation value. When selecting one of the edges with the largest MI values for v , the corresponding focus diagrams between u and v show similar but not identical correlation structures. Overall, correlations in v are slightly higher and more equally distributed over the individual height layers, which is visible due to a larger amount of highly saturated edges.

6 CONCLUSION AND FUTURE WORK

We have proposed the use of importance-based correlation sampling to support an interactive focus+context visualization of correlation structures in large 3D ensemble fields. The maximum correlation between two sub-regions is estimated via Bayesian optimal sampling, and region-to-region maxima are visualized via a chord diagram including edge bundling to reduce visual clutter. For large ensembles which do not fit into GPU memory, maxima are sampled from a mean-tree at a suitable resolution. Regions are linearized along a space-filling curve and mapped to the circular chord layout. The user can interactively select chord edges for a closer inspection in a focus view, and analyse correlation patterns of more than one physical variable via a chord

diagram or an inter-variable correlation matrix. We have further introduced optimized GPU solutions to efficiently compute prominent measures of statistical dependence in large ensembles. The use of our approach has been demonstrated with two large simulation ensembles and one synthetic data set.

A limitation of using chord diagrams is that for more than one variable the visualization becomes cluttered and edges occlude each other. Nevertheless, we believe that by using two distinct colors as proposed, in combination with the possibility to filter correlations and brick pairs, the user can effectively analyse two variables. Using more than two variables, however, becomes increasingly difficult. By juxtaposition of the chord diagrams for different variables, the major differences in the correlation structures can be conveyed efficiently, yet it is clear that this doesn’t scale to the analysis of many variables. Therefore, in the future we intend to analyse the use of set operations, i.e., set intersections, between the set of initial edges of different fields. We believe that by using such operations also similarities and differences between the correlation structures in multiple fields can be conveyed effectively.

Furthermore, we intend to extend the proposed approach in the following ways. Firstly, it will be interesting to include temporal correlations into chord diagrams. This, however, is challenging, since it requires to encode the time dimension into the diagrams and access far more data for correlation sampling. The first challenge can be addressed by using an additional circular shell around the chords in which the time axis is encoded, and in which the user can select the times that should be considered for correlation analysis. The second challenge requires the extension of the mean-tree to also cover the time domain, so that interactivity can be ensured when both spatial sub-regions and time points are selected adaptively.

Secondly, we will collaborate with domain experts from meteorology to explore unknown correlation structures in large weather forecast ensembles. So far, such structures are not considered in meteorological workflows due to computational limits, even though there is agreement that they

could hint at unknown relationships. Such relationships can, for instance, show dependencies between different simulation variables or between initial fields that have been assimilated and those that are simulated. Alternatively, they could be used to reduce the number of ensemble members that need to be simulated, since some of them carry redundant information. In this context, we consider in particular the analysis of the temporal evolution of correlation structures to be important.

SUPPLEMENTAL MATERIALS

The code of the software implementing the visualization and interaction technique proposed in this work is made available at <https://github.com/chrismile/Corrender> and archived at [74]. The used synthetic correlation test data set can be generated with a script available in the GitHub repository of the application. Access to the convective-scale 1000 ensemble member simulation forecast by Necker et al. [1] used in this work can be requested from the authors of the data set. The data set by Matsunobu et al. [73] is publically available.

REFERENCES

- [1] T. Necker, S. Geiss, M. Weissmann, J. Ruiz, T. Miyoshi, and G.-Y. Lien, "A convective-scale 1,000-member ensemble simulation and potential applications," *Quarterly Journal of the Royal Meteorological Society*, vol. 146, no. 728, pp. 1423–1442, 2020. [Online]. Available: <https://rmets.onlinelibrary.wiley.com/doi/abs/10.1002/qj.3744>
- [2] D. Holten, "Hierarchical edge bundles: Visualization of adjacency relations in hierarchical data," *IEEE Transactions on Visualization and Computer Graphics*, vol. 12, no. 5, pp. 741–748, 2006.
- [3] C.-K. Chen, C. Wang, K.-L. Ma, and A. T. Wittenberg, "Static correlation visualization for large time-varying volume data," in *2011 IEEE Pacific Visualization Symposium*, 2011, pp. 27–34.
- [4] M. Rautenhaus, M. Kern, A. Schäfler, and R. Westermann, "Three-dimensional visualization of ensemble weather forecasts – part 1: The visualization tool met.3d (version 1.0)," *Geoscientific Model Development*, vol. 8, no. 7, p. 2329–2353, 2015.
- [5] H. Obermaier and K. I. Joy, "Future challenges for ensemble visualization," *IEEE Computer Graphics and Applications*, vol. 34, no. 3, pp. 8–11, 2014.
- [6] J. Wang, S. Hazarika, C. Li, and H.-W. Shen, "Visualization and visual analysis of ensemble data: A survey," *IEEE Transactions on Visualization and Computer Graphics*, vol. 25, no. 9, pp. 2853–2872, 2019.
- [7] I. Demir, M. Jarema, and R. Westermann, "Visualizing the central tendency of ensembles of shapes," in *SIGGRAPH ASIA 2016 Symposium on Visualization*, ser. SA '16. New York, NY, USA: Association for Computing Machinery, 2016. [Online]. Available: <https://doi.org/10.1145/3002151.3002165>
- [8] F. Ferstl, M. Kanzler, M. Rautenhaus, and R. Westermann, "Visual analysis of spatial variability and global correlations in ensembles of iso-contours," *Computer Graphics Forum*, vol. 35, no. 3, pp. 221–230, 2016. [Online]. Available: <https://onlinelibrary.wiley.com/doi/abs/10.1111/cgf.12898>
- [9] A. T. Pang, C. M. Wittenbrink, and S. K. Lodha, "Approaches to uncertainty visualization," *The Visual Computer*, vol. 13, no. 8, pp. 370–390, Nov 1997. [Online]. Available: <https://doi.org/10.1007/s003710050111>
- [10] J. Sanyal, S. Zhang, J. Dyer, A. Mercer, P. Amburn, and R. Moorhead, "Noodles: A tool for visualization of numerical weather model ensemble uncertainty," *IEEE Transactions on Visualization and Computer Graphics*, vol. 16, no. 6, pp. 1421–1430, 2010.
- [11] R. T. Whitaker, M. Mirzargar, and R. M. Kirby, "Contour boxplots: A method for characterizing uncertainty in feature sets from simulation ensembles," *IEEE Transactions on Visualization and Computer Graphics*, vol. 19, no. 12, pp. 2713–2722, 2013.
- [12] S. Hazarika, A. Biswas, and H.-W. Shen, "Uncertainty visualization using copula-based analysis in mixed distribution models," *IEEE Transactions on Visualization and Computer Graphics*, vol. 24, no. 1, pp. 934–943, 2018.
- [13] T. Nocke, S. Buschmann, J. F. Donges, N. Marwan, H.-J. Schulz, and C. Tominski, "Review: visual analytics of climate networks," *Nonlinear Processes in Geophysics*, vol. 22, no. 5, pp. 545–570, 2015. [Online]. Available: <https://npg.copernicus.org/articles/22/545/2015/>
- [14] D. S. Wilks, "The stippling shows statistically significant grid points: How research results are routinely overstated and overinterpreted, and what to do about it," *Bulletin of the American Meteorological Society*, vol. 97, no. 12, pp. 2263 – 2273, 2016. [Online]. Available: <https://journals.ametsoc.org/view/journals/bams/97/12/bams-d-15-00267.1.xml>
- [15] F. Ferstl, M. Kanzler, M. Rautenhaus, and R. Westermann, "Visual analysis of spatial variability and global correlations in ensembles of iso-contours," *Computer Graphics Forum*, vol. 35, no. 3, pp. 221–230, 2016. [Online]. Available: <https://onlinelibrary.wiley.com/doi/abs/10.1111/cgf.12898>
- [16] C. Dalelane, K. Winderlich, and A. Walter, "Evaluation of global teleconnections in CMIP6 climate projections using complex networks," *Earth System Dynamics*, vol. 14, no. 1, pp. 17–37, 2023. [Online]. Available: <https://esd.copernicus.org/articles/14/17/2023/>
- [17] A. Kumpf, M. Rautenhaus, M. Riemer, and R. Westermann, "Visual analysis of the temporal evolution of ensemble forecast sensitivities," *IEEE Transactions on Visualization and Computer Graphics*, vol. 25, no. 1, pp. 98–108, 2019.
- [18] B. Ancell and G. J. Hakim, "Comparing adjoint- and ensemble-sensitivity analysis with applications to observation targeting," *Monthly Weather Review*, vol. 135, no. 12, pp. 4117 – 4134, 2007. [Online]. Available: <https://journals.ametsoc.org/view/journals/mwre/135/12/2007mwr1904.1.xml>
- [19] R. D. Torn and G. J. Hakim, "Ensemble-based sensitivity analysis," *Monthly Weather Review*, vol. 136, no. 2, pp. 663 – 677, 2008. [Online]. Available: <https://journals.ametsoc.org/view/journals/mwre/136/2/2007mwr2132.1.xml>
- [20] M. Evers, M. Böttinger, and L. Linsen, "Interactive Visual Analysis of Regional Time Series Correlation in Multi-field Climate Ensembles," in *Workshop on Visualisation in Environmental Sciences (EnvirVis)*. The Eurographics Association, 2023.
- [21] P. Laarne, E. Amnell, M. A. Zaidan, S. Mikkonen, and T. Nieminen, "Exploring non-linear dependencies in atmospheric data with mutual information," *Atmosphere*, vol. 13, no. 7, 2022. [Online]. Available: <https://www.mdpi.com/2073-4433/13/7/1046>
- [22] M. S. Babel, G. B. Badgujar, and V. R. Shinde, "Using the mutual information technique to select explanatory variables in artificial neural networks for rainfall forecasting," *Meteorological Applications*, vol. 22, no. 3, pp. 610–616, 2015. [Online]. Available: <https://rmets.onlinelibrary.wiley.com/doi/abs/10.1002/met.1495>
- [23] Y. Ning, G. Liang, W. Ding, X. Shi, Y. Fan, J. Chang, Y. Wang, B. He, and H. Zhou, "A mutual information theory-based approach for assessing uncertainties in deterministic multi-category precipitation forecasts," *Water Resources Research*, vol. 58, no. 11, p. e2022WR032631, 2022, e2022WR032631. [Online]. Available: <https://agupubs.onlinelibrary.wiley.com/doi/abs/10.1029/2022WR032631>
- [24] X. He, Y. Tao, Q. Wang, and H. Lin, "Multivariate spatial data visualization: A survey," *Journal of Visualization*, vol. 22, no. 5, pp. 897–912, 2019.
- [25] N. Sauber, H. Theisel, and H.-P. Seidel, "Multifield-graphs: An approach to visualizing correlations in multifield scalar data," *IEEE Transactions on Visualization and Computer Graphics*, vol. 12, no. 5, pp. 917–924, 2006.
- [26] L. Gosink, J. Anderson, W. Bethel, and K. Joy, "Variable interactions in query-driven visualization," *IEEE Transactions on Visualization and Computer Graphics*, vol. 13, no. 6, pp. 1400–1407, 2007.
- [27] S. Nagaraj, V. Natarajan, and R. S. Nanjundiah, "A gradient-based comparison measure for visual analysis of multifield data," *Computer Graphics Forum*, vol. 30, no. 3, pp. 1101–1110, 2011. [Online]. Available: <https://onlinelibrary.wiley.com/doi/abs/10.1111/j.1467-8659.2011.01959.x>
- [28] Z. Zhang, K. T. McDonnell, E. Zadok, and K. Mueller, "Visual correlation analysis of numerical and categorical data on the correlation map," *IEEE Transactions on Visualization and Computer Graphics*, vol. 21, no. 2, pp. 289–303, 2015.

- [29] X. Liu and H.-W. Shen, "Association analysis for visual exploration of multivariate scientific data sets," *IEEE Transactions on Visualization and Computer Graphics*, vol. 22, no. 1, pp. 955–964, 2016.
- [30] A. Biswas, S. Dutta, H.-W. Shen, and J. Woodring, "An information-aware framework for exploring multivariate data sets," *IEEE Transactions on Visualization and Computer Graphics*, vol. 19, no. 12, pp. 2683–2692, 2013.
- [31] L. Wang, X. Tang, J. Zhang, and D. Guan, "Correlation analysis for exploring multivariate data sets," *IEEE Access*, vol. 6, pp. 44 235–44 243, 2018.
- [32] M. Berenjkoub, R. O. Monico, R. S. Laramée, and G. Chen, "Visual analysis of spatio-temporal relations of pairwise attributes in unsteady flow," *IEEE Transactions on Visualization and Computer Graphics*, vol. 25, no. 1, pp. 1246–1256, 2019.
- [33] T. Pfaffmoser and R. Westermann, "Visualization of global correlation structures in uncertain 2d scalar fields," in *Computer Graphics Forum*, vol. 31, no. 3pt2. Wiley Online Library, 2012, pp. 1025–1034.
- [34] T. Liebmann, G. H. Weber, and G. Scheuermann, "Hierarchical correlation clustering in multiple 2d scalar fields," *Computer Graphics Forum*, vol. 37, no. 3, pp. 1–12, 2018. [Online]. Available: <https://onlinelibrary.wiley.com/doi/abs/10.1111/cgf.13396>
- [35] M. Evers, K. Huesmann, and L. Linsen, "Uncertainty-aware Visualization of Regional Time Series Correlation in Spatio-temporal Ensembles," *Computer Graphics Forum*, 2021.
- [36] Y. Su, G. Agrawal, J. Woodring, A. Biswas, and H.-W. Shen, "Supporting correlation analysis on scientific datasets in parallel and distributed settings," in *Proceedings of the 23rd International Symposium on High-Performance Parallel and Distributed Computing*, ser. HPDC '14. New York, NY, USA: Association for Computing Machinery, 2014, p. 191–202. [Online]. Available: <https://doi.org/10.1145/2600212.2600230>
- [37] D. Hilbert, "Über die stetige abbildung einer line auf ein flächenstück," *Mathematische Annalen*, vol. 38, p. 459–460, 1891.
- [38] L. Zhou, C. R. Johnson, and D. Weiskopf, "Data-driven space-filling curves," *IEEE Transactions on Visualization and Computer Graphics*, vol. 27, no. 2, pp. 1591–1600, 2021.
- [39] I. Demir, C. Dick, and R. Westermann, "Multi-charts for comparative 3d ensemble visualization," *IEEE Transactions on Visualization and Computer Graphics*, vol. 20, no. 12, pp. 2694–2703, 2014.
- [40] C. Wang, H. Yu, R. W. Grout, K.-L. Ma, and J. H. Chen, "Analyzing information transfer in time-varying multivariate data," in *2011 IEEE Pacific Visualization Symposium*, 2011, pp. 99–106.
- [41] J. Weissenböck, B. Fröhler, E. Gröller, J. Kastner, and C. Heinzl, "Dynamic volume lines: Visual comparison of 3d volumes through space-filling curves," *IEEE Transactions on Visualization and Computer Graphics*, vol. 25, no. 1, pp. 1040–1049, 2019.
- [42] D. Rees, R. S. Laramée, P. Brookes, and T. D'Cruze, "Interaction techniques for chord diagrams," in *2020 24th International Conference Information Visualisation (IV)*, 2020, pp. 28–37.
- [43] J. Bae and K. Lee, "Tagreel: A visualization of tag relations among user interests in the social tagging system," in *2009 Sixth International Conference on Computer Graphics, Imaging and Visualization*, 2009, pp. 437–442.
- [44] L. Gou and X. Zhang, "Treenetviz: Revealing patterns of networks over tree structures," *Visualization and Computer Graphics, IEEE Transactions on*, vol. 17, pp. 2449 – 2458, 01 2012.
- [45] J. H. Halton, "Algorithm 247: Radical-inverse quasi-random point sequence," *Commun. ACM*, vol. 7, no. 12, pp. 701–702, Dec. 1964. [Online]. Available: <http://doi.acm.org/10.1145/355588.365104>
- [46] M. Roberts, "The unreasonable effectiveness of quasirandom sequences," <http://extremelarning.com.au/unreasonable-effectiveness-of-quasirandom-sequences/>, 2018, accessed: 2023-03-20.
- [47] R. E. Caflisch, "Monte carlo and quasi-monte carlo methods," *Acta Numerica*, vol. 7, p. 1–49, 1998.
- [48] J. Mockus, *Bayesian Approach to Global Optimization: Theory and Applications*. Dordrecht: Springer Netherlands, 1989. [Online]. Available: <https://doi.org/10.1007/978-94-009-0909-0>
- [49] R. Garnett, *Bayesian Optimization*. Cambridge University Press, 2023.
- [50] E. Brochu, V. M. Cora, and N. de Freitas, "A tutorial on bayesian optimization of expensive cost functions, with application to active user modeling and hierarchical reinforcement learning," *CoRR*, vol. abs/1012.2599, 2010. [Online]. Available: <http://arxiv.org/abs/1012.2599>
- [51] J. Gablonsky and C. Kelley, "A locally-biased form of the direct algorithm," *Journal of Global Optimization*, vol. 21, pp. 27–37, 01 2001.
- [52] S. G. Johnson, "The NLOpt nonlinear-optimization package," <http://github.com/stevengj/nlopt>, 2023, accessed: 2023-05-04.
- [53] B. Matérn, *Spatial Variation: Stochastic Models and Their Application to Some Problems in Forest Surveys and Other Sampling Investigations*. Meddelanden fran Statens Skogsforskningsinstitut, 1960.
- [54] S. Daulton, X. Wan, D. Eriksson, M. Balandat, M. A. Osborne, and E. Bakshy, "Bayesian optimization over discrete and mixed spaces via probabilistic reparameterization," in *Advances in Neural Information Processing Systems*, 2022. [Online]. Available: <https://realworldml.github.io/files/cr/paper22.pdf>
- [55] A. Cully, K. Chatzilygeroudis, F. Allocati, and J.-B. Mouret, "Limbo: A Flexible High-performance Library for Gaussian Processes modeling and Data-Efficient Optimization," *The Journal of Open Source Software*, vol. 3, no. 26, p. 545, 2018.
- [56] T. M. Cover and J. A. Thomas, *Entropy, Relative Entropy, and Mutual Information*. John Wiley & Sons, Ltd, 2005, ch. 2, pp. 13–55. [Online]. Available: <https://onlinelibrary.wiley.com/doi/abs/10.1002/047174882X.ch2>
- [57] M. Teßmann, C. Eisenacher, F. Enders, M. Stamminger, and P. Has-treiter, "GPU accelerated normalized mutual information and b-spline transformation," in *Eurographics Workshop on Visual Computing for Biomedicine*. The Eurographics Association, 2008.
- [58] R. Shams, P. Sadeghi, R. Kennedy, and R. Hartley, "Parallel computation of mutual information on the GPU with application to real-time registration of 3d medical images," *Computer Methods and Programs in Biomedicine*, vol. 99, no. 2, pp. 133–146, 2010. [Online]. Available: <https://www.sciencedirect.com/science/article/pii/S0169260709002946>
- [59] V. Saxena, J. Rohrer, and L. Gong, "A parallel GPU algorithm for mutual information based 3d nonrigid image registration," in *Euro-Par 2010 - Parallel Processing*. Berlin, Heidelberg: Springer Berlin Heidelberg, 2010, pp. 223–234.
- [60] J. Öfverstedt, J. Lindblad, and N. Sladoje, "Fast computation of mutual information in the frequency domain with applications to global multimodal image alignment," *Pattern Recognition Letters*, vol. 159, pp. 196–203, 2022. [Online]. Available: <https://www.sciencedirect.com/science/article/pii/S0167865522001817>
- [61] A. Kraskov, H. Stögbauer, and P. Grassberger, "Estimating mutual information," *Phys. Rev. E*, vol. 69, p. 066138, Jun 2004. [Online]. Available: <https://link.aps.org/doi/10.1103/PhysRevE.69.066138>
- [62] E. W. Weisstein, "Digamma function," <https://mathworld.wolfram.com/DigammaFunction.html>, 2002, from MathWorld—A Wolfram Web Resource. Accessed: 2023-03-25.
- [63] D. Wehr and R. Radkowski, "Parallel kd-tree construction on the GPU with an adaptive split and sort strategy," *International Journal of Parallel Programming*, vol. 46, no. 6, pp. 1139–1156, Dec 2018. [Online]. Available: <https://doi.org/10.1007/s10766-018-0571-0>
- [64] I. Wald, "A stack-free traversal algorithm for left-balanced k-d trees," 2022.
- [65] M. Kern, C. Neuhauser, T. Maack, M. Han, W. Usher, and R. Westermann, "A comparison of rendering techniques for 3d line sets with transparency," *IEEE Transactions on Visualization and Computer Graphics*, vol. 27, no. 8, pp. 3361–3376, 2021.
- [66] C. A. R. Hoare, "Algorithm 64: Quicksort," *Commun. ACM*, vol. 4, no. 7, p. 321, Jul. 1961. [Online]. Available: <https://doi.org/10.1145/366622.366644>
- [67] D. R. Musser, "Introspective sorting and selection algorithms," *Software: Practice and Experience*, vol. 27, no. 8, pp. 983–993, 1997. [Online]. Available: <https://onlinelibrary.wiley.com/doi/abs/10.1002/%28SICI%291097-024X%28199708%2927%3A8%3C983%3A%3AAID-SPE117%3E3.0.CO%3B2-%23>
- [68] The Free Software Foundation, "The GNU C++ library," <https://gcc.gnu.org/onlinedocs/libstdc++/libstdc++-html-USERS-4.4/a01027.html>, 2009, accessed: 2023-08-08.
- [69] C. Lanczos, "A precision approximation of the gamma function," *Journal of the Society for Industrial and Applied Mathematics Series B Numerical Analysis*, vol. 1, no. 1, pp. 86–96, 1964. [Online]. Available: <https://doi.org/10.1137/0701008>
- [70] V. T. Toth, "The gamma function," <https://www.rskey.org/CMS/index.php/the-library/11>, 2012, accessed: 2023-03-20.
- [71] C. de Boor, "Subroutine package for calculating with b-splines." Los Alamos National Lab, United States, Tech. Rep., 1971. [Online]. Available: <https://www.osti.gov/biblio/4740859>

- [72] M. Mononen, “NanoVG,” <https://github.com/memononen/nanovg>, 2022, accessed: 2023-03-23.
- [73] T. Matsunobu, C. Keil, and C. Barthlott, “ICON-D2 microphysically perturbed ensemble simulations including initial and boundary condition uncertainty,” *LMU Munich, Faculty of Physics*, 2022.
- [74] C. Neuhauser and J. Stumpfegger, “chrismile/Correrender: A correlation field renderer using the Vulkan graphics API, v2023-08-09,” Aug. 2023. [Online]. Available: <https://doi.org/10.5281/zenodo.8228651>

7 BIOGRAPHY SECTION



Christoph Neuhauser is a PhD candidate at the Computer Graphics and Visualization Group at the Technical University of Munich (TUM). He received his Bachelor's and Master's degrees in computer science from TUM in 2019 and 2020. Major interests in research comprise scientific visualization and real-time rendering.



Josef Stumpfegger is a Scientific Programmer at the Technical University of Munich, where he obtained his B.Sc. and M.Sc. in computer science in 2019 and 2021. His major interests in research are scientific data visualization for large-scale data, real-time rendering and high performance GPU computing.



Rüdiger Westermann studied computer science at the Technical University Darmstadt and received his Ph.D. in computer science from the University of Dortmund, both in Germany. In 2002, he was appointed the chair of Computer Graphics and Visualization at TUM. His research interests include scalable data visualization and simulation algorithms, GPU computing, real-time rendering of large data, and uncertainty visualization.